The International Journal of Advanced Manufacturing Technology
https://doi.org/10.1007/s00170-024-13570-3

ORIGINAL ARTICLE

Dynamic mechanical properties of selective laser-melted AlSi10Mg lattice structures: experimental and numerical analysis with emphasis on Johnson-Cook model parameters

Mustafa Caliskan[1] · Hakan Hafizoglu[2] · Nazim Babacan[3]

Received: 19 September 2023 / Accepted: 29 March 2024

Abstract
Additively manufactured lattice structures are extensively utilized because of their unique characteristics, including lightweight design, high energy absorption capabilities, and exceptional specific strength. This study focuses on accurately simulating the dynamic mechanical behavior of AlSi10Mg lattice structures produced using selective laser melting (SLM). A series of experimental studies has been conducted to establish the parameters of the J–C hardening and damage model for additively manufactured AlSi10Mg alloys. The lattice structures, featuring face-centered cubic (FCC) and diamond topologies with a 25% designed relative density, underwent scanning electron microscopy (SEM) for geometrical precision assessment. Dynamic compressive behavior was investigated via split Hopkinson pressure bar (SHPB) tests. Numerical simulations in Ls-Dyna, utilizing the identified J–C parameters, were employed to replicate SHPB tests. Findings indicate that the specific strength and the specific energy absorption values of FCC lattice samples have higher than those of diamond samples at strain rates of 750 and 1100 s^{-1}. While the overall strains and deformation modes were well predicted by numerical analyzes, a deeper insight into local stress concentrations under dynamic loads was achieved. Consequently, the obtained J–C model parameters offer valuable insight into characterizing the dynamic behavior of AlSi10Mg lattice structures produced by SLM.

Keywords Additive manufacturing · Selective laser melting · AlSi10Mg · Lattice structures · Dynamic mechanical behavior · Finite element method

1 Introduction

Additive manufacturing technology, which facilitates the production of computer-designed objects by sequentially layering materials, has been rapidly developing and becoming widespread in recent years [1, 2]. Laser powder bed fusion, also referred as selective laser melting (SLM) is one of the metal additive manufacturing method that enables obtaining products by melting metal powders with laser in powder bed systems. In this technology, a laser beam melts the metal powder along a specified path and performs this process in each layer. The advantages of SLM technology are often used in the production of complex structures, such as lattice structures, that are challenging to produce using traditional methods. The design flexibility inherent in SLM has prompted researchers to concentrate on optimizing the performance of geometrically intricate lattice structures [3–5]. Lattice structures stand out as extensively utilized porous arrangements across a wide array of applications due to their exceptional combination of high specific strength, rigidity, and capacity to absorb energy [6–9].

The performance of lattice structures under both static and dynamic loads has undergone comprehensive investigation across numerous studies [10–19]. For instance, Platek et al. [10] conducted an in-depth examination wherein they subjected 316L steel lattice structures to both quasi-static and dynamic compression tests. Their findings revealed that lattice structures effectively absorb and distribute dynamic effects, positioning themselves as viable components for passive protection systems. Additionally, Tancogne-Dejean

✉ Nazim Babacan
nazimbabacan@sivas.edu.tr

[1] Institute of Defense Technologies, Sivas University of Science and Technology, 58100 Sivas, Turkey

[2] TUBITAK Defense Industries Research and Development Institute, 06261 Ankara, Turkey

[3] Department of Mechanical Engineering, Sivas University of Science and Technology, 58100 Sivas, Turkey

Published online: 17 April 2024

et al. [11] conducted dynamic experimental analyses on 316L alloy lattice structures and observed these materials to possess a notable energy absorption capacity across various loading directions. Ozdemir et al. [12] characterized the quasi-static and particularly dynamic load deformation behavior of Ti6Al4V alloy lattice structures. Their employment of split Hopkinson pressure bar (SHPB) tests demonstrated that lattice structures efficiently distribute impact loads in a timely manner and mitigate the peak impact stress.

Among the alloys commonly processed using SLM, aluminum alloys, known for their balanced combination of strength and ductility, exhibit higher energy absorption capabilities compared to high-strength alloys in specific circumstances [20–22]. Notably, the AlSi10Mg alloy, distinguished by its remarkable mechanical attributes within the realm of aluminum alloys, is one of the few alloys that is widely produced with SLM [23–26].

One of the most important tools to predict the mechanical behavior of the complex structures is the finite element method (FEM). FEM studies have a great place in the literature and industry to solve the engineering problems which requires long efforts and costly experiments to perform. FE modeling of additively manufactured samples has also gained popularity, particularly in predicting the dynamic absorption properties [10, 27, 28] and machining performance [29–32]. By considering the effects of strain rate, temperature, and pressure on the material's response, Johnson–Cook material and damage model (J–C model) is well-suited for simulating and analyzing complex dynamic phenomena [33]. The findings in the literature suggest that employing the J–C model allows for the customization of lattice specimens and facilitates the control and optimization of cutting performance in additively manufactured specimens.

In addition to the studies conducted with traditional J–C material model, there have been other researches which numerically investigated behavior of additively manufactured materials with other material models. One of these studies was performed by Tancogne-Dejean et al. [28]. They modeled high strain rate tension and compression response of stainless steel 316L fabricated through SLM in conjunction with a modified JC material model. They declared that the numerical results obtained by modified JC model was in good agreement with the compression test results. In another study by Mahbod and Asgari [34], compression responses of additively manufactured functionally graded porous materials were simulated using Ls-Dyna software. In their proposed numerical model, the structures were simulated with plastic-kinematic material model implemented in Ls-Dyna software. In a study by Gebhardt et al. [35], AlSi10Mg alloy rhombic dodecahedron lattice structures fabricated with SLM were numerically modeled in terms of tension, compression, and shear and torsion loading conditions with Abaqus software. Researchers in that study used isotropic elastic-plastic material model with von Mises yield surface and isotropic hardening. They concluded that the material model successfully predicted the responses of the specimens under all the loading conditions aforementioned above.

Literature review showed that even though there have been other material models to model dynamic behavior of lattice structures, traditional J–C material model is one of the most efficient and simple material model owing to its ability to simulate plastic strain with triaxiality [36–38]. A limited number of investigations have been conducted to establish the J–C material model parameters specific to additive manufacturing of AlSi10Mg alloys [39–41]. However, it is noteworthy that the damage parameters within this model were absent in the studies by Maconachie et al. [40] and Akturk et al. [41]. Additionally, Nirmal et al. [39] utilized the FEM simulations to deduce these parameters. Nevertheless, comprehensive experimental investigations aimed at identifying the constants of the J–C material and failure model for AlSi10Mg alloys produced by SLM are lacking in the literature.

The dynamic mechanical properties studies of the AlSi10Mg porous structures are rarely found. Hou et al. [42] recently examined the energy absorption properties of AlSi10Mg structures featuring triply periodic minimal surfaces (TPMS) across different strain rates by using SHPB. In another study, Maconachie et al. [38] explored the dynamic characteristics of the body-centered cubic (BCC)–based and face-centered cubic (FCC)–based AlSi10Mg structures. Nonetheless, their study utilized relatively modest strain rates within the range of 100 s^{-1}. Therefore, there is still a need to examine the dynamic mechanical properties of the AlSi10Mg lattice alloys which can be particularly effective at absorbing and dissipating impact energy during crashes, collisions, or ballistic penetration. To address these gaps, in this study, J–C material and failure model parameters of AlSi10Mg alloy produced by SLM were obtained by utilizing series of experimental tests. The lattice structures were designed with FCC and diamond topologies. By subjecting these structures to dynamic compression tests at varying strain rates using SHPB tests and numerical analyses, their dynamic compressive behavior is thoroughly explored.

2 Material and methods

2.1 Fabrication of the bulk samples and their mechanical tests

The manufacturing process using selective laser melting (SLM) involved the utilization of spherical metal powder ERMAK A461-AlSi10Mg (15-50 µm). Employing the ENAVISION 250 SLM device (ERMAKSAN, Turkey), all

samples were manufactured using processing parameters including a 320-W laser power, 100-µm hatch distance, 800-mm/s scanning speed, and 30-µm layer thickness under an argon gas atmosphere.

To identify the J–C model parameters, bulk tensile and compression tests were conducted, subjecting them to both quasi-static and dynamic conditions. For quasi-static tensile testing, cylindrical tensile specimens were fabricated in accordance with ASTM E8/E8M [43], featuring a gauge length measuring 20 mm and a gauge diameter of 4 mm. The samples were clamped at an 8-mm diameter, and their overall length was 55 mm. Furthermore, the notched tensile testing specimens were manufactured employing identical overall dimensions. Notch radii of R, 1 mm, 2 mm, and 5 mm were applied. Figure 1(a–d) present three-dimensional perspectives of the design for the samples subjected to quasi-static tensile testing. These specimens were tested at room temperature (approx. 20 °C) and a reference strain rate (10^{-3} s^{-1}) using an Autograph AG-IS-100 kN tensile testing machine (Shimadzu, Japan), as depicted in Fig. 1(e).

In preparation for the dynamic compression tests, cylindrical compression samples measuring Ø6 × 8 mm^2 were manufactured. Similarly, for the high temperature dynamic tests, tension specimens were produced to align with the device's tensile heads, with a gauge length diameter and length of 6.35 mm and 13.7 mm, respectively. Figure 2(a) shows a portion of SLMed tensile specimens produced for both quasi-static and dynamic tests before detachment from the substrate, along with their respective supports.

Utilizing a split Hopkinson pressure bar (SHPB) test setup (as schematically shown in Fig. 2(b)), a series of dynamic compression and tensile tests are conducted at various strain rates and temperatures. Dynamic compression tests were performed at room temperature, encompassing strain rates of 600, 1100, and 1800 s^{-1}. Moreover, split Hopkinson compression tests were executed at 100, 200, and 300 °C with a constant strain rate of 600 s^{-1}. The SHPB tensile tests were applied under strain rates of 750, 1000, and 1400 s^{-1} at room temperature, and similarly, at a strain rate of 1000 s^{-1} tensile tests at temperatures of 100 and 150 °C were

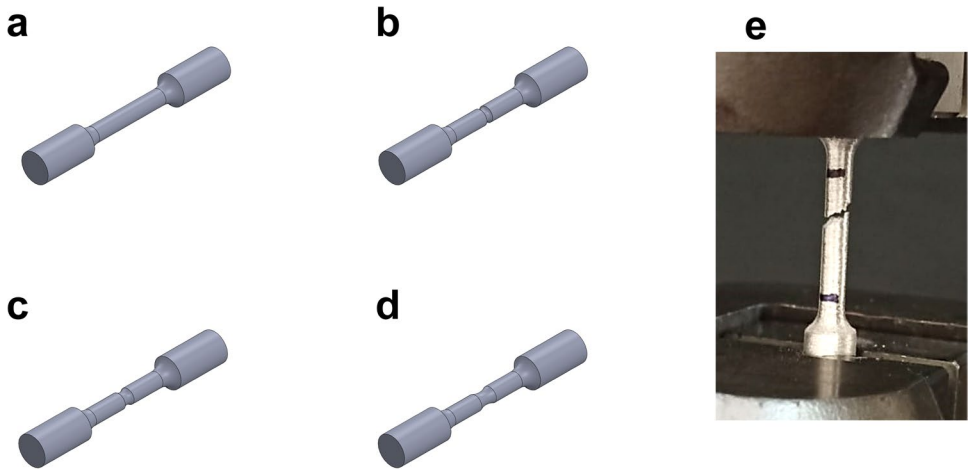

Fig. 1 Quasi-static tensile test samples **a** unnotched (standard), **b** $R = 1$, **c** $R = 3$, and **d** $R = 5$. **e** An image captured following a quasi-static test of an unnotched sample

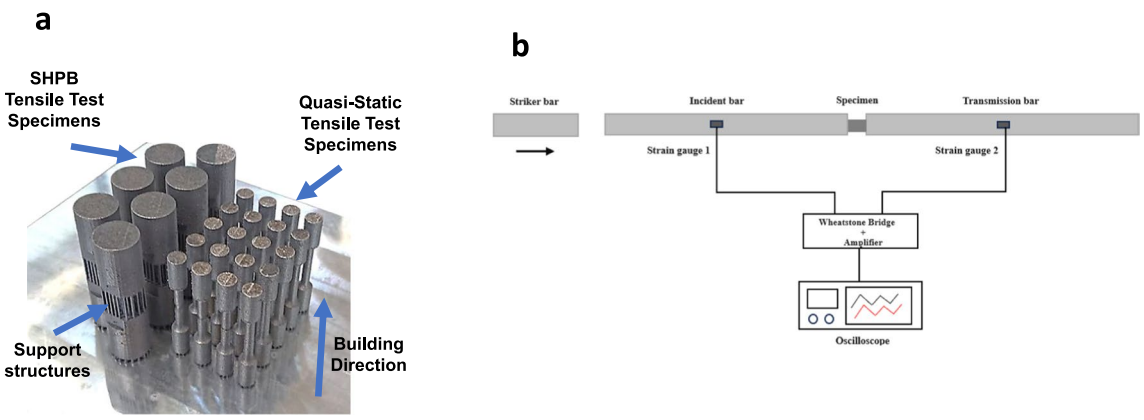

Fig. 2 **a** A view of the unnotched and notched tensile test specimens for the quasi-static tests (on the right) and the split Hopkinson pressure bar (SHPB) tensile test specimens (on the left) on top of the build substrate. **b** A schematic view of the SHPB test setup

employed. All quasi-static and dynamic mechanical tests were applied by using three samples from each condition.

2.2 Design and fabrication of the lattice structures and their dynamic tests

To examine the dynamic properties and verify the J–C model properties through numerical studies, lattice samples with a unit cell size of 4 mm and overall dimensions of 12 × 12 ×12 mm^3 were digitally designed in lattice structures. The face-centered cubic (FCC) and diamond topologies, were created using Solidworks software. Computer-aided design (CAD) representations of these samples can be observed in Fig. 3. For the FCC and diamond lattice structures, the strut diameters of these parts were configured as 1.09 mm and 0.97 mm, respectively, to achieve relative densities of 25%. The samples were manufactured using the identical processing parameters outlined in Section 2.1 through the process of SLM.

For the computation of the effective relative density of the samples, measurements of width, thickness, and height were taken for each manufactured specimen using a caliper. Utilizing these measurements, the total volume of the samples was determined, enabling the calculation of their apparent densities through division by the sample mass. Then, the experimental relative densities were determined by dividing the calculated apparent densities by the material density of 2.67 g/cm^3.

High strain rate compression tests were conducted at room temperature on two specimens each to explore the dynamic mechanical behaviors of FCC and diamond lattice structures fabricated through SLM. These tests were performed at strain rates of 750 and 1100 s^{-1} using the SHPB test configuration. Imaging of the lattice structures was carried out both before (as-built) and after the dynamic compression tests by utilizing a MIRA3 XMU scanning electron microscope (SEM) (TESCAN, Czech Republic).

2.3 FEM model of the SHPB test setup

A robust representation of the SHPB test setup was developed to simulate dynamic compression experiments conducted on lattice structures within the Ls-Dyna software. The simulation involved a mesh structure consisting of a total of 174,424 and 155,152 elements for the FCC and diamond lattice simulations, respectively, including Hopkinson bars in hexahedral structure and lattices in tetrahedron structure. In these investigations, a uniform element size of 0.4 mm was used for the FCC and diamond lattice structures. Meanwhile, the striker, incident, and transmission bars were modeled using an element size of 3 mm. The initial velocity values acquired from the experimental SHPB device are assigned to the striker as the governing boundary condition.

The J–C model was employed, integrating parameters established in this study (detailed in Section 3.1) for the lattice structures fabricated using SLM with AlSi10Mg alloy powder. Lattice structures were modeled with 15-JOHNSON–COOK material model. Hopkinson bars, on the other hand, are elastically modeled with 01-ELASTIC material model by using 7.85 kg/m^3 density, 210 GPa modulus of elasticity, and 0.3 Poisson ratio values of C350 steel. The schematic representation of the generated numerical model is shown in Fig. 4.

In numerical models, contacts between bars and bar/sample were described by means of AUTOMATIC_SINGLE_SURFACE.

3 Results and discussion

3.1 Determination of J–C hardening model parameters

The Johnson–Cook (J–C) hardening model characterizes how a material responds mechanically under varying rates of strain and temperatures. The stress-strain relationship

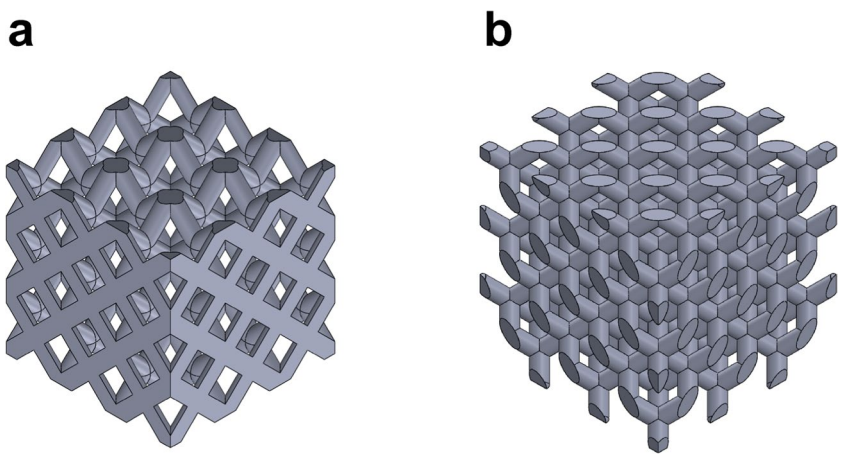

Fig. 3 CAD views of lattice structures: **a** FCC and **b** diamond

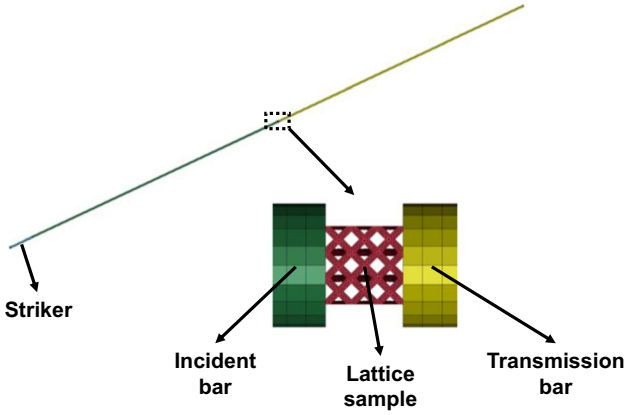

Fig. 4 Schematic representation of the numerical model created for the dynamic compression tests performed with the SHPB test setup

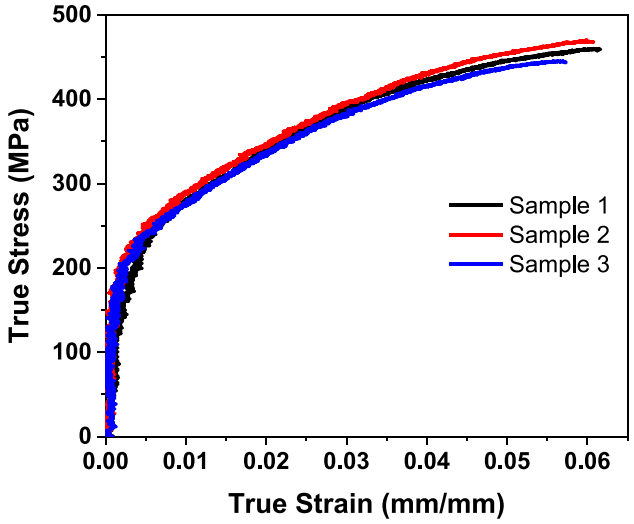

Fig. 5 True stress-strain curves derived from the quasi-static tensile testing of standard tensile specimens

describing the plastic behavior of the material is represented as Eq. (1) [44–47].

$$\sigma = \left[A + B{\varepsilon_p}^n\right]\left[1 + C\ln\left(\frac{\dot{\varepsilon}}{\dot{\varepsilon}_0}\right)\right]\left[1 - (T^*)^m\right] \quad (1)$$

where A is initial yield strength of the material at reference strain rate and reference temperature. B and n denote the strain hardening modulus and strain hardening constants, respectively. While C represents the strain rate hardening parameter, m is the thermal softening coefficient. σ is the equivalent plastic stress, and ε_p represents the accumulated plastic strain. $\dot{\varepsilon}$ and $\dot{\varepsilon}_0$ correspond to the test strain rate and reference strain rate, respectively. Lastly, T^* relates to the homologous temperature, and it is found with Eq. (2):

$$T^* = \frac{T - T_0}{T_m - T_0} \quad (2)$$

where T, T_0, and T_m are test, reference, and melting temperature, respectively.

3.1.1 Determination of parameters *A*, *B* and *n*

When the test was done at the reference strain rate and reference temperature which were specified as 10^{-3} s^{-1} and 298 K in this study, Eq. (1) can be modified as Eq. (3):

$$\sigma = \left[A + B{\varepsilon_p}^n\right] \quad (3)$$

The true stress-strain curves depicting the unnotched standard specimens subjected to quasi-static tensile testing are shown in Fig. 5. Evidently, reproducible results were achieved across all three samples, and the average values derived from these curves were employed for parameter calculations. It is worth noting that although only one representative curve out of the three is presented hereafter, all calculations were conducted using the average values.

Herein, the yield stress value of 251.45 MPa acquired from Fig. 5 corresponds to the value denoted as A. Upon reordering Eq. (3) following the derivation of parameter A, Eq. (4) is obtained.

$$\ln(\sigma - A) = \ln(B) + n\ln\left(\varepsilon_p\right) \quad (4)$$

The parameter n is determined by the slope of the regression line formed by plotting $\ln(\varepsilon_p)$ (in x axis) against $\ln(\sigma - A)$ (in y axis). Consequently, a value $n = 0.68$ was computed. Upon substituting the acquired A and n parameters into Eq. (4), B value was computed as 1664.61 MPa.

3.1.2 Determination of parameter *C*

To obtain the parameter C (strain rate hardening parameter), the true stress-strain curves were generated through dynamic compression tests. These SPHB tests are done at 600, 1100, and 1800 s^{-1} at the room temperature, and the resulting stress-strain curves, as well as the reference strain curve, are presented in Fig. 6(a). The mechanical properties derived from these curves are also shown in Fig. 6(b). It is evident that the yield and ultimate compressive strength values, as well as the fracture strains, exhibited an increase with higher strain rates. Notably, the fracture strain values showed approximately threefold increase when the strain rate escalated from 10^{-3} s^{-1} to 1800 s^{-1}.

Because all the tests aimed at determining the C parameter were conducted at room temperature, Eq. (5), derived from Eq. (1), was employed.

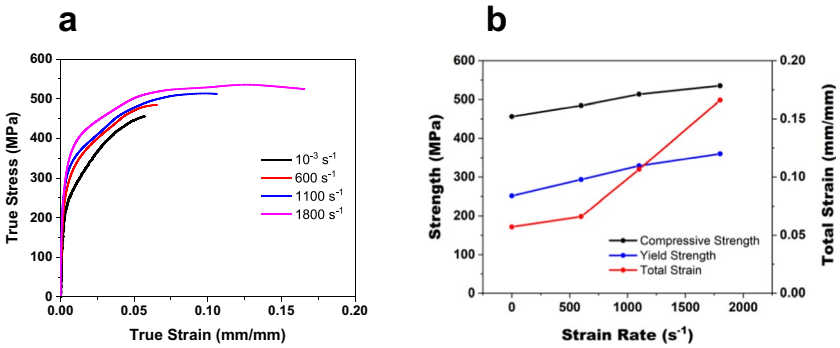

Fig. 6 **a** True stress-strain curves obtained as a result of compression tests performed at different strain rates. **b** Yield, compressive strength, and fracture strain values obtained from **a**

$$\sigma = \left[A + B\varepsilon_p{}^n\right]\left[1 + C\ln\left(\frac{\dot{\varepsilon}}{\dot{\varepsilon}_0}\right)\right] \tag{5}$$

C was computed as 0.00605 using stress values and accumulated plastic strain at 0.02 true strain values, which varied based on the strain rate. A curve-fitting approach involving non-linear regression was employed on the data points in the form of $\ln\left(\frac{\dot{\varepsilon}}{\dot{\varepsilon}_0}\right)$ (x axis) $-\frac{\sigma}{\left[A+B\varepsilon_p{}^n\right]} - 1$ (y axis) to find parameter C.

3.1.3 Determination of parameter *m*

To compute the parameter m within the J–C material model, the true stress-strain curves shown in Fig. 7(a) are utilized. These curves were derived from tests conducted at varying temperatures (100, 200, and 300 °C) with a constant strain rate of 600 s^{-1}. The yield stress, ultimate compressive stress, and total strain values extracted from these curves are illustrated in Fig. 7(b). As expected, the strengths exhibited a decline, while the total strain value showed an increase with higher strain rates.

By plugging in the previously calculated A, B, n, and C parameters into Eq. (1), and through a non-linear curve-fitting process involving stress variations at different temperatures, the value of m was determined to be 0.835.

3.2 Determination of J–C damage parameters

Following the computation of all the parameters within the J–C hardening model for the SLM-produced AlSi10Mg alloy, the corresponding parameters of the J–C damage model, defined by Eq. (6) [48, 49], were subsequently determined.

$$\varepsilon_f = \left[D_1 + D_2\exp\left(D_3\sigma^*\right)\right]\left[1 + D_4\ln(\frac{\dot{\varepsilon}}{\dot{\varepsilon}_0})\right]\left[1 + D_5T^*\right] \tag{6}$$

D_1 to D_5 in Eq. (6) represent J–C damage model parameters. In addition, ε_f stands for fracture strain, and σ^* is the stress triaxiality ratio. According to Bridgman's formula [50, 51], σ^* can be calculated by using Eq. (7):

$$\sigma^* = \frac{1}{3} + \ln\left(1 + \frac{d_i}{4R}\right) \tag{7}$$

where d_i is the initial diameter of the sample, and R corresponds to the notch radii.

3.2.1 Determination of parameters D_1, D_2, and D_3

The formulation of Eq. (6) applicable to tests conducted at room temperature and at the reference strain rate, fracture strain value can be written as Eq. (8):

$$\varepsilon_f = \left[D_1 + D_2\exp\left(D_3\sigma^*\right)\right] \tag{8}$$

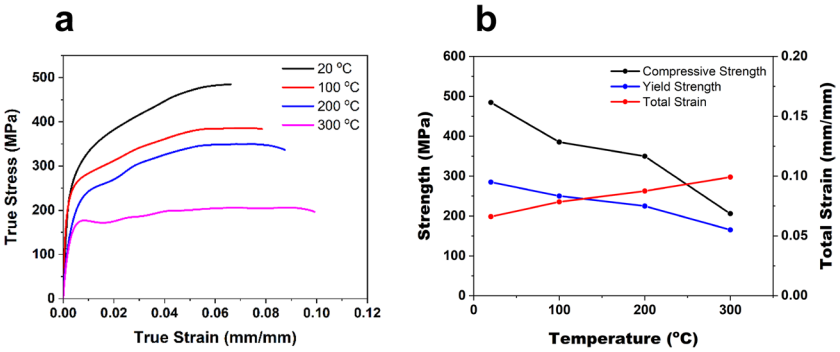

Fig. 7 True stress-strain graphs derived from compression tests conducted under various temperatures at a strain rate of 600 s^{-1}. **b** Yield, compressive strength and fracture strain values obtained from **a**

By employing Eq. (7), σ^* values of the notched samples $R1$, $R2$, and $R5$ were computed as 0.908, 0.661, and 0.478, respectively. The σ^* value of the unnotched sample is 1/3. The fracture strain (ε_f) is a parameter dependent on the initial (d_i) and final diameters (d_f) of the tensile specimen post-testing. Its mathematical expression is provided in Eq. (9):

$$\varepsilon_f = 2\ln\left(\frac{d_i}{d_f}\right) \tag{9}$$

d_f value of the samples was ascertained through image processing of the tensile test specimens after the tests. After conducting tests at the reference strain rate and room temperature, the first three damage parameters were determined based on the fracture strains that varied according to the σ^* (stress triaxiality factor), in accordance with Eq. (8). The $\sigma^* - \varepsilon_f$ graph is illustrated in Fig. 8, and the values of $D_1 = 1.047$, $D_2 = -0.965$, and $D_3 = 0.0432$ were obtained using a non-linear regression algorithm.

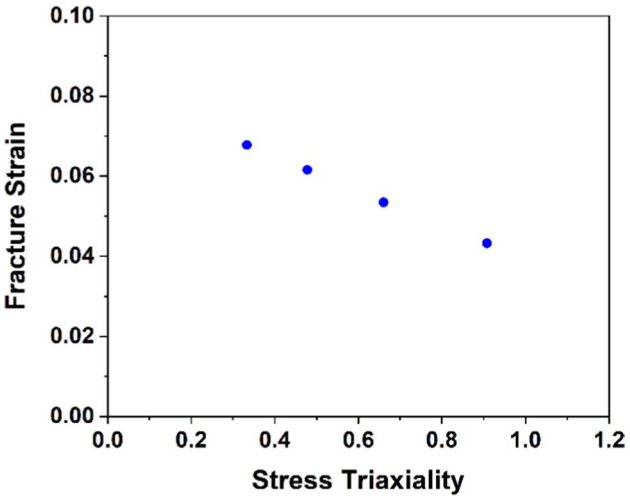

Fig. 8 ε_f (fraction strain) values as a function of σ^* (stress triaxiality factor)

3.2.2 Determination of parameter D_4 and D_5

Equation (10) is derived by rearranging Eq. (6) for tests conducted at various strain rates (750, 1000, and 1400 s^{-1}) and room temperature:

$$\varepsilon_f = \left[D_1 + D_2 \exp\left(D_3\sigma^*\right)\right]\left[1 + D_4 \ln\left(\frac{\dot{\varepsilon}}{\dot{\varepsilon}_0}\right)\right] \tag{10}$$

The calculation of d_f values rely on image processing of high-speed camera captures shown in Fig. 9 which were obtained immediately after the fracture of the tensile samples. These values were then used to find ε_f using Eq. (9). Subsequently, the damage parameters obtained in the previous section (Sec. 3.2.1) were substituted and calculated as $D_4 = 0.0205$ by a non-linear curve fitting method based on the fracture strains of the unnotched tensile specimens, which vary depending on the different strain rates.

To calculate the parameter D_5, the initial step involved determining T^* (homologous temperature) values through Eq. (2), utilizing the tensile test temperatures of 20, 100, and 150 °C. Subsequently, by substituting the damage parameters D_1 to D_4, along with values for σ^* of 1/3 (for unnotched tensile specimens), $\dot{\varepsilon}$ of 1000 s^{-1} (constant strain rate value for high temperature tests), T^* and the ε_f (calculated from Eq. (9)) into Eq. (6), a curve fitting procedure led to the determination of D_5 as 0.785.

Finally, all J–C material and damage parameters for the AlSi10Mg alloy, produced using SLM, have been derived from calculations based on experimental data. These parameters are tabulated in Table 1.

3.3 Dimensional accuracy of the lattice structures

Additively manufactured diamond and FCC samples were firstly investigated through SEM images to evaluate both the dimensional and morphological characteristics of the struts. Figure 10 shows the SEM images focused on the

Fig. 9 The perspectives of the tensile specimens within the SPHB test configuration after the dynamic experiments at strain rates of **a** 750, **b** 1000, and **c** 1400 s^{-1}

Table 1 Experimentally identified Johnson–Cook material and damage model parameters for selective laser melted AlSi10Mg alloy

A	251.45
B	1664.61
n	0.68
C	0.00605
m	0.835
D_1	1.047
D_2	−0.965
D_3	0.0432
D_4	0.0205
D_5	0.785

lattice test specimens and the visual depiction of the unit cells belonging to the diamond and FCC lattice structures. It is seen that the structural integrity is successfully preserved.

To ascertain disparities between the intended and fabricated strut diameters, a minimum of 10 strut diameter measurements were conducted on selected regions of the manufactured samples using the Image J software. Table 2 provides details of the strut diameters specified for each lattice structure, accompanied by the mean and standard deviation values derived from measurements in experimental production. Additionally, the measured relative densities are also included.

Evident from this data, structures with strut diameters exceeding the intended dimensions were fabricated. The variance amounts to approximately 50 µm for both topologies. In the process of SLM fabrication, incomplete or partial fusion of powder particles can be observed, as depicted in Fig. 10(c, f). This occurrence leads to an enlargement of the produced strut diameters beyond the intended specifications, a phenomenon documented in various studies [6, 27, 52, 53]. Consequently, the effective relative densities surpass the original design values by a slight margin.

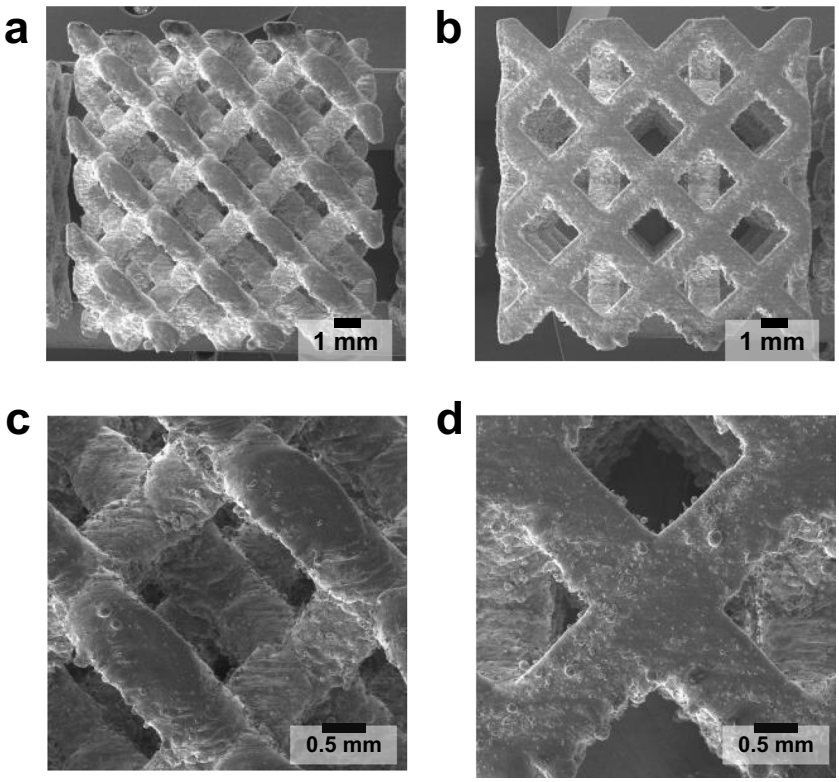

Fig. 10 SEM images from SLM-generated lattice structures: **a** and **c** Diamond, **b** and **d** FCC lattice structures

Table 2 Comparison of strut diameter and relative density values obtained through measurements from SEM images with the designed values

	Designed strut diameter (mm)	Measured strut diameter (mm)	Designed relative density (%)	Measured relative density (%)
Diamond	0.97	1.01 ± 0.07	24.85	27.46 ± 0.34
FCC	1.09	1.14 ± 0.05	25.00	27.25 ± 0.44

3.4 Experimental dynamic mechanical response of the lattice structures

In this section, the dynamic mechanical properties of the FCC and diamond lattice structures produced via SLM under high strain rates were investigated. To achieve this, compression tests on two samples from each lattice structure using the SHPB test configuration were conducted at two different strain rates (750 and 1100 s^{-1}). The samples were oriented within the test setup to ensure that the applied force was parallel to their respective building directions in SLM to align with the methodology employed in bulk sample testing. Figure 11 represents the views of the non-tested and tested samples. While the FCC structure underwent primary compression from both its lower and upper layers, a more uniform crushing pattern was detected in the diamond structure.

Figure 12a and b show the complete set of stress-strain plots acquired at strain rates of 750 and 1100 s^{-1}, respectively. Notably, these curves exhibit remarkable proximity among samples of the same lattice type, indicating consistent quality across the production of samples sharing similar lattice characteristics.

Upon comparing the sample types, it becomes evident that the FCC lattice demonstrates superior compressive strength. The highest compressive strength, approximately 37 MPa, was consistently observed at both strain rates for FCC samples. These findings demonstrate that, in terms of dynamic mechanical response, the selection of topology holds significant importance, even when the relative densities of the designs are equivalent.

Average specific strength and specific energy absorption values are calculated by considering the sample masses, and

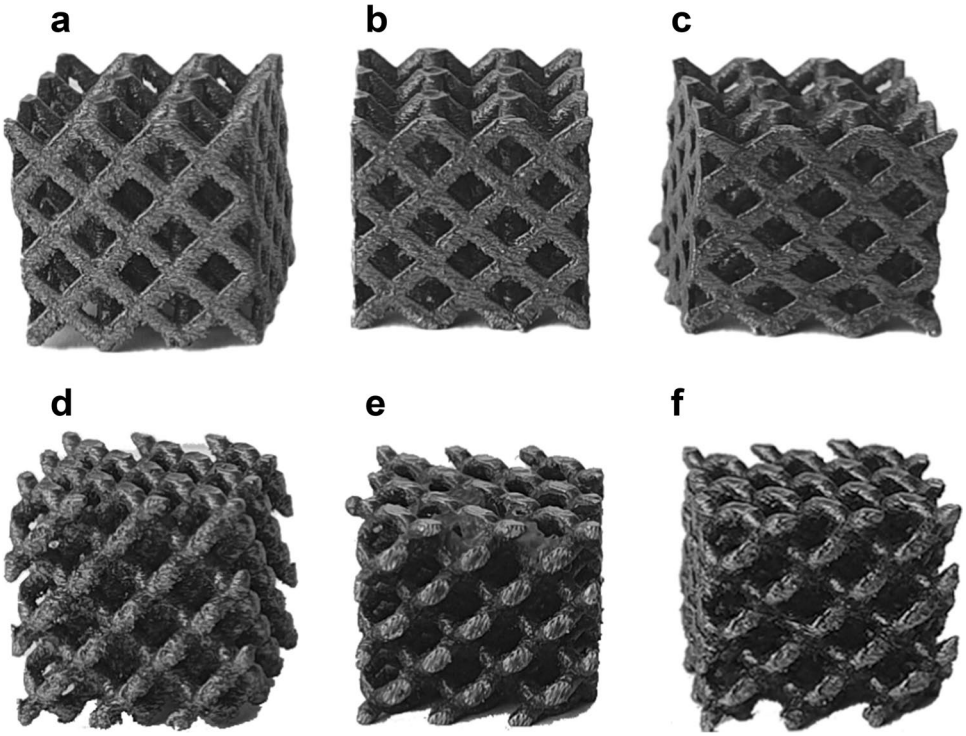

Fig. 11 Non-tested and tested **a**, **b**, and **c** FCC and **d**, **e**, and **f** diamond samples: **a**, **b**, **c**, and **d** non-tested, **b** and **e** tested at a strain rate of 750 s^{-1}, and **c**, **d**, **e**, and **f**) tested at a strain rate of 1100 s^{-1}

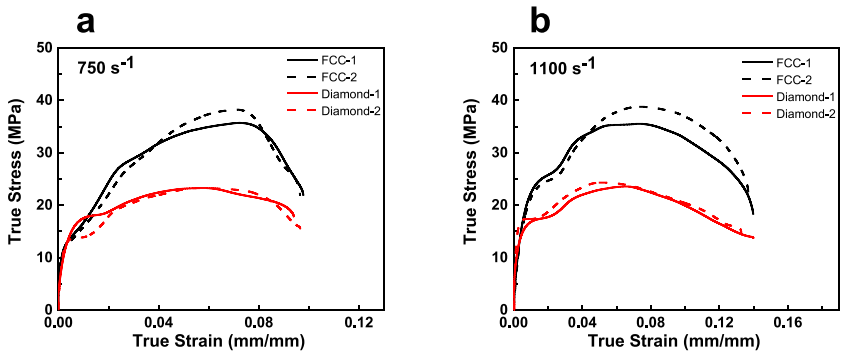

Fig. 12 True stress-strain graphs obtained as a result of dynamic compression tests performed on lattice structures at **a** 750 and **b** 1100 s^{-1} strain rate

the results are shown in Fig. 13(a) and (b), respectively. Analyzing the data from Fig. 13(a), it is apparent that the peak compressive strength values remain consistent for the same lattice type across strain rates of 750 and 1100 s^{-1}. However, as strain rate magnifies, the material displayed more ductile characteristics, as evidenced by Fig. 12(a) and (b). Peak strength and failure occurred at higher strains for the samples deformed at higher strain rate. Therefore, the higher strain rate led to elevated specific energy absorption for both lattice topologies due to the increase in the ductility of the samples (Fig. 13(b)).

The dynamic mechanical behavior of the AlSi10Mg FCC lattice structure, designed with an approximate relative density of 7%, was investigated by Maconachie et al. [38]. The results indicated a specific compressive strength of around 15 kPa/(kg/m^3) for this sample, which was compressed under the strain rate of 133 s^{-1}. Notably, this value constitutes around 30% of the specific compressive strength determined for the same lattice structure with a designed relative density of 25%, subjected to compression at strain rates of 750 and 1100 s^{-1} in the present study. This discrepancy in specific compressive strength highlights the notable impact of relative density and strain rate on the mechanical behavior of FCC lattice structures. However, as the strain rate increase did not affect the specific strength values prominently in this study, it can be said that the dominant influence on these outcomes is primarily attributable to the relative density rather than the variation in strain rate.

3.5 Numerical dynamic mechanical response of the lattice structures and verification of J–C parameters

The experimental dynamic studies were replicated numerically by using a developed finite element model (FEM). This model was created using the J–C model parameters acquired and introduced in Sections 3.1 and 3.2. In the numerical analyses, computer-aided design (CAD) geometries of the lattice structures imported into the model. Thus, instead of comparing the total deformation values in the compression direction between experimental and numerical studies, strain values were compared. Both experimental and numerical results of the SHPB compression test applied to the FCC and diamond lattice structures are presented in Table 3.

The numerical strain values acquired at a deformation rate of 1100 s^{-1} exhibit a remarkable proximity to the corresponding experimental strain values, showing an approximation error of merely around 2%. For the numerical analyses at a deformation rate of 750 s^{-1}, an approximate 15% error is obtained in comparison to the experimental values.

The strain rate in the numerical tests is derived by extracting strain values from the middle sections of both the incident bar and transmission bar, arranged in a configuration similar to the placement of strain gauges illustrated in Fig. 2(b)). The approach is rooted in 1D wave propagation theory, utilizing signals obtained from strain gauges attached to the bars. The strain rate as a function of time was calculated using the following formula:

$$\dot{\varepsilon}(t) = -\frac{2C_0}{L_0}\varepsilon_r(t) \tag{11}$$

Here, C_0 is the elastic wave speed in the bar; L_0 is the length of the specimen. $\varepsilon_r(t)$ is the reflected wave, calculated from the difference between the transmitted and incident

Table 3 Comparison of the experimental and numerical results of SHPB compression tests on samples with FCC and diamond topologies

		Strain rate (s^{-1})	Strain (mm/mm)	Numerical error (%)
FCC	**Exp.**	750	0.0822	12.77
	FEM	750	0.0717	
	Exp.	1100	0.1059	2.27
	FEM	1100	0.1083	
Diamond	**Exp.**	750	0.0711	16.03
	FEM	750	0.0825	
	Exp.	1100	0.1284	2.02
	FEM	1100	0.1258	

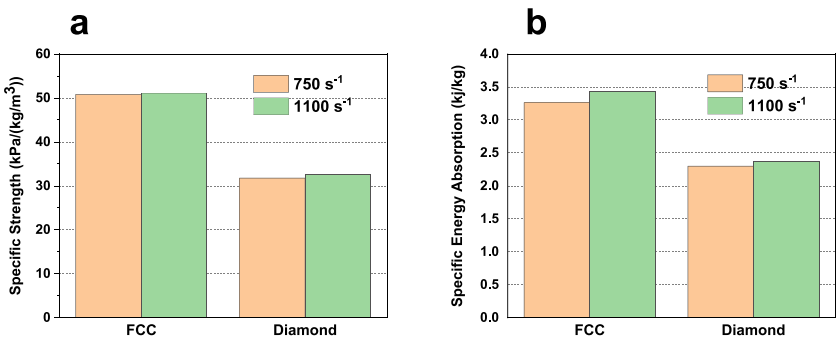

Fig. 13 **a** The specific strength and **b** specific energy absorption values resulting from the SHPB tests based on different lattice structures

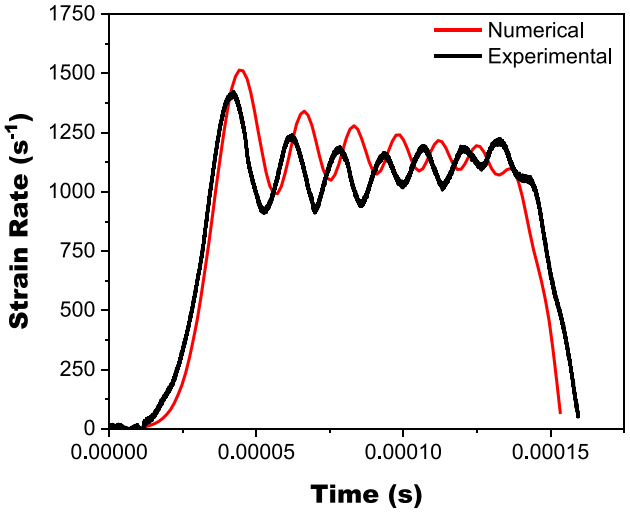

Fig. 14 Curves showing the relationship between strain rate and time derived from both experimental and numerical tests at a strain rate of 1100 s^{-1}

waves. Figure 14 shows the comparison between the strain rate values over time for the numerical and experimental SHPB tests on an FCC structure at a strain rate of 1100 s^{-1}. Although the experimental values are slightly lower than the experimental values, potentially attributed to the omission of losses induced by friction, the close alignment of the curves affirms the similarity between the numerical and experimental tests.

Through the application of FEM, it becomes feasible to analyze the alterations in internal stress within the structure as the structure undergoes loading. The internal stresses at various deformation levels during the dynamic compression test conducted at 1100 s^{-1} are presented for FCC and diamond structure in Fig. 15 and Fig. 16, respectively. For both lattice structures, it is obvious from both figures that the highest stresses were obtained as the compression wave traveled along the lattice structures (Fig. 15(b) and Fig. 16(b)). In the case of the FCC structure, immediately following the approach of compression wave to incident bar/sample interface, the highest stresses were observed on the outer surfaces of the connecting region where two diagonal struts meet. As the compression wave traveled through the structure (Fig. 15(b)) during compression, maximum von Mises stress increased for the entire structure about 92%. FCC sample reaches a steady state (Fig. 15(c)) after some time with the equivalent stress nearly the same as with the one in Fig. 15(b). In all three deformation stages, it is seen that the maximum internal stress values were concentrated in the junction points of the struts. At other parts of the lattice

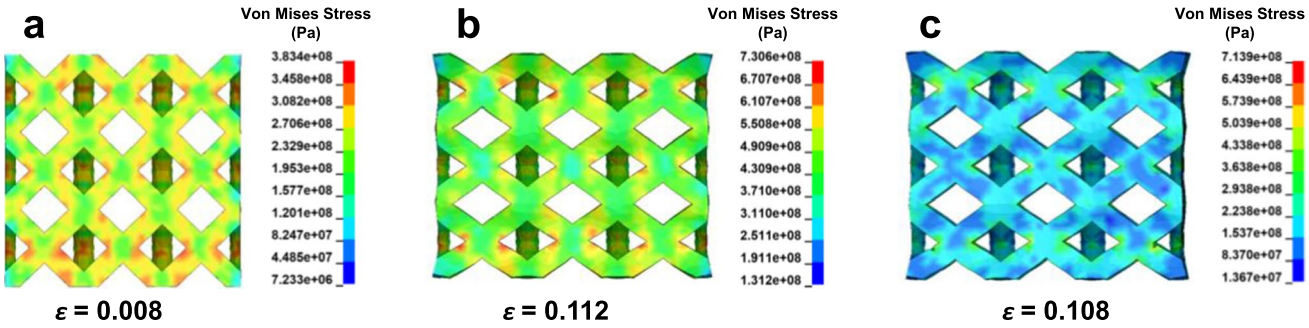

Fig. 15 Equivalent stress evolution across the FCC lattice structure during the numerical SHPB test at 1100 s^{-1}

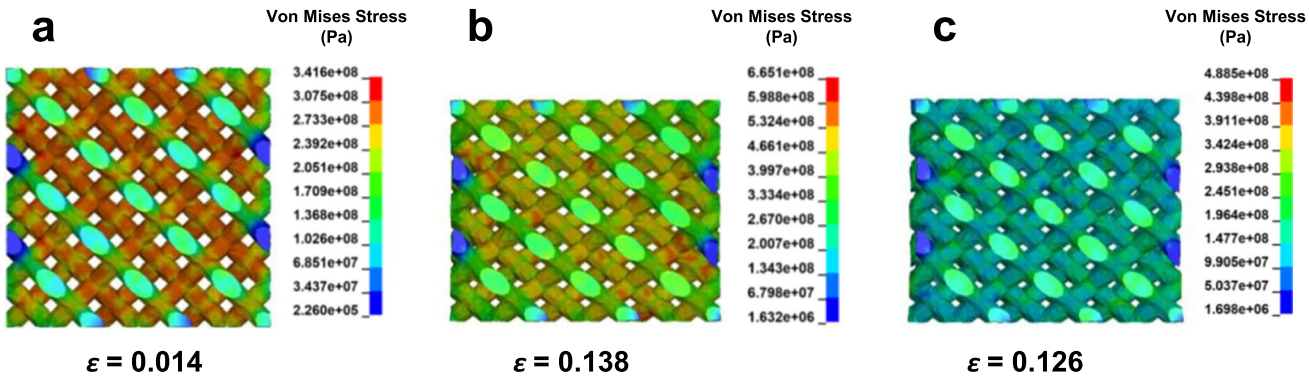

Fig. 16 Equivalent stress evolution across the diamond lattice structure during the numerical SHPB test at 1100 s^{-1}

structure, aside from junction points, the stress levels tended to increase at the beginning of the deformation and decrease at the end of compression process as the sample reached a steady state.

For the case of diamond lattice structure, unlike FCC structure, it can be seen from Fig. 16 that the stress distributes more uniformly all around the structure during the entire compression process. In the middle stage of the deformation when compression wave traveled along the sample (Fig. 16(b)), the maximum stress increased approximately 95% compared to the first stage. In the steady state stage after the middle stage, the peak stress decreased by about 27%. The uniform stress distribution in the diamond structure might lead to lower peak stresses in the diamond structure without any crack formation compared to FCC structures.

After the SHPB compression tests at a deformation rate of 1100 s^{-1} for both FCC and diamond structures, comparative SEM images and numerical analysis results are presented, respectively, in Figs. 17 and 18. In the case of the FCC structure, the tests revealed that the maximum stress occurs at the junction points of the struts. This phenomenon has been previously observed in compression tests of FCC structures [38, 54]. Both experimental and numerical investigations indicated the presence of small cracks at the junctions of struts close to the surfaces where the FCC structure interacts with the split Hopkinson bars, as indicated by the red arrows. A similar observation was made in the study conducted by Maconachie et al. [38] under dynamic loads, suggesting its association with stress wave propagation.

Upon examining the images shown in Fig. 18, captured after conducting the experimental and numerical tests on the diamond structure, it can be observed that, unlike the FCC structure, no crack-like damage occurred. Instead, only compression in the direction of the sample is evident. Consequently, the deformation pattern obtained from the numerical analysis closely resembles the experimental results. Furthermore, it is noteworthy that the stresses obtained from the numerical analysis of the diamond structure distributed more uniformly across all struts in the lattice, in contrast to

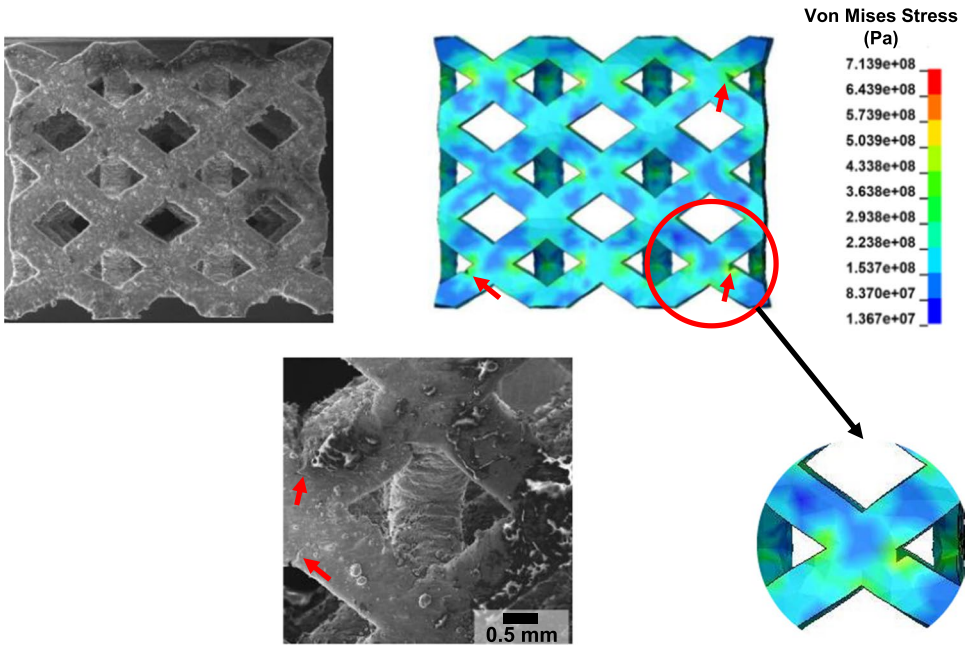

Fig. 17 Experimental and numerical post-test views of the FCC sample tested at a strain rate of 1100 s^{-1}

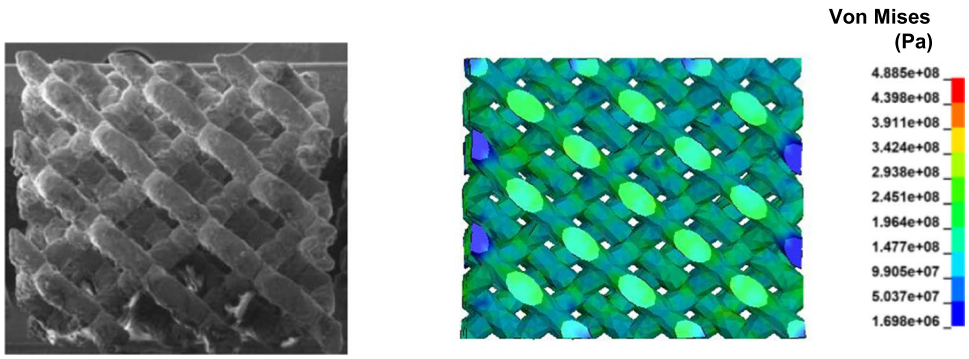

Fig. 18 Experimental and numerical post-test views of the diamond sample tested at a strain rate of 1100 s^{-1}

the stress concentration observed in specific regions as in the FCC structure. This different deformation behavior of the diamond topology is sourced from its diagonally intersecting struts in three dimensions which may disperse the applied load more uniformly.

The way the diamond structure reacts to dynamic loads holds potential significance, particularly in scenarios involving more dynamic tests like ballistic penetration. In those scenarios, the diamond structure's ability to exhibit a more uniform response and evenly distribute the resulting stresses throughout its configuration, as opposed to the FCC structure, could play a role in enhancing its overall performance.

4 Conclusion

In this study, the dynamic mechanical properties of selective laser melted AlSi10Mg lattice structures were investigated, employing both experimental and numerical analyses. The primary findings can be summarized as follows:

1. Model parameters of Johnson–Cook (J–C) material and damage model ($A = 251.45$ MPa, $B = 1664.61$ MPa, $n = 0.68$, $C = 0.00605$, $m = 0.835$; $D_1 = 1.047$, $D_2 = -0.965$, $D_3 = 0.0432$, $D_4 = 0.0205$, $D_5 = 0.785$) for additively manufactured AlSi10Mg were determined based on quasi-static tensile tests, split Hopkinson pressure bar (SHPB) tensile, and compression tests of the bulk samples conducted at various temperatures.
2. The face-centered cubic (FCC) and diamond AlSi10Mg lattice structures were produced by selective laser melting (SLM), aiming for a 25% designed relative density. While the strut diameters being approximately 0.05 mm larger than the intended design, measured relative density of the samples were about 27.5%. This variance can be attributed to incomplete or partial fusion of powder particles on the surfaces, as evident from SEM observations.
3. The compressive dynamic mechanical behavior of the FCC and diamond AlSi10Mg lattice structured was characterized at strain rates of 750 and 1100 s^{-1} using the SHPB tests. The increase in strain rate did not affect the specific strength values prominently, but only an increment in ductility was observed. Notably, the FCC structures demonstrated higher specific strength and specific energy absorption values in comparison to the diamond samples.
4. The finite element model (FEM) simulation SHPB tests of additively manufactured AlSi10Mg implemented by the determined J–C model parameters effectively replicated the observed deformation behavior and resultant strains from experimental investigations. Consequently, this model holds promise for designing optimal geometric configurations of AlSi10Mg that could be well-suited for dynamic protective applications, such as ballistic armor, a subject scheduled for future investigations.

Acknowledgements The authors are very grateful to Ahmet Sever from Ermaksan Machinery Industry and Trade Inc. (Bursa/Turkey) for producing the test samples.

Author contribution Hakan Hafizoglu and Nazim Babacan contributed to the study conception and design. Material preparation, data collection, and analysis were performed by Mustafa Caliskan and Hakan Hafizoglu. The first draft of the manuscript was written by Mustafa Caliskan and Nazim Babacan, and all the authors commented on the previous versions of the manuscript.

Funding Open access funding provided by the Scientific and Technological Research Council of Türkiye (TÜBİTAK). This work was supported by the Scientific and Technological Research Council of Turkey (TÜBİTAK) under Grant No. 221M604.

Declarations

Ethics approval Not applicable.

Consent to participate Not applicable.

Consent for publication All the authors have agreed to the authorship, read, and approved the manuscript, and given consent for submission and subsequent publication of the manuscript. The authors guarantee that the contribution to the work has not been previously published elsewhere.

Competing interests The authors declare no competing interests.

References

1. Cooke S, Ahmadi K, Willerth S, Herring R (2020) Metal additive manufacturing: technology, metallurgy and modelling. J Manuf Process 57:978–1003. https://doi.org/10.1016/j.jmapro.2020.07.025
2. Trevisan F, Calignano F, Lorusso M et al (2017) On the selective laser melting (SLM) of the AlSi10Mg alloy: process, microstructure, and mechanical properties. Materials 10:76. https://doi.org/10.3390/ma10010076
3. Gümrük R, Mines RAW (2013) Compressive behaviour of stainless steel micro-lattice structures. Int J Mech Sci 68:125–139. https://doi.org/10.1016/j.ijmecsci.2013.01.006

4. Zhang B, Han X, Chen C et al (2021) Effect of the strut size and tilt angle on the geometric characteristics of selective laser melting AlSi10Mg. Rapid Prototyp J 27:879–889. https://doi.org/10.1108/RPJ-08-2020-0187
5. Yu T, Hyer H, Sohn Y et al (2019) Structure-property relationship in high strength and lightweight AlSi10Mg microlattices fabricated by selective laser melting. Mater Des 182:108062. https://doi.org/10.1016/j.matdes.2019.108062
6. Mazur M, Leary M, Sun S et al (2016) Deformation and failure behaviour of Ti-6Al-4V lattice structures manufactured by selective laser melting (SLM). Int J Adv Manuf Technol 84:1391–1411. https://doi.org/10.1007/s00170-015-7655-4
7. Gangireddy S, Komarasamy M, Faierson EJ, Mishra RS (2019) High strain rate mechanical behavior of Ti-6Al-4V octet lattice structures additively manufactured by selective laser melting (SLM). Mater Sci Eng A 745:231–239. https://doi.org/10.1016/j.msea.2018.12.101
8. Yang C, Li QM (2020) Advanced lattice material with high energy absorption based on topology optimisation. Mech Mater 148:103536. https://doi.org/10.1016/j.mechmat.2020.103536
9. Pirinu A, Primo T, Del A et al (2023) Mechanical behaviour of AlSi10Mg lattice structures manufactured by the selective laser melting (SLM). Int J Adv Manuf Technol 124:1651–1680. https://doi.org/10.1007/s00170-022-10390-1
10. Platek P, Sienkiewicz J, Janiszewski J, Jiang F (2020) Investigations on mechanical properties of lattice structures with different values of relative density made from 316L by selective laser melting (SLM). Materials 13:2204. https://doi.org/10.3390/ma13092204
11. Tancogne-dejean T, Spierings AB, Mohr D (2016) Additively-manufactured metallic micro-lattice materials for high specific energy absorption under static and dynamic loading. Acta Mater 116:14–28. https://doi.org/10.1016/j.actamat.2016.05.054
12. Ozdemir Z, Hernandez-Nava E, Tyas A et al (2016) Energy absorption in lattice structures in dynamics: experiments. Int J Impact Eng 89:49–61. https://doi.org/10.1016/j.ijimpeng.2015.10.007
13. Li Z, Nie Y, Liu B et al (2020) Mechanical properties of AlSi10Mg lattice structures fabricated by selective laser melting. Mater Des 192:108709. https://doi.org/10.1016/j.matdes.2020.108709
14. Maskery I, Aremu AO, Simonelli M et al (2015) Mechanical properties of Ti-6Al-4V selectively laser melted parts with body-centred-cubic lattices of varying cell size. Exp Mech 55:1261–1272. https://doi.org/10.1007/s11340-015-0021-5
15. Leary M, Mazur M, Williams H et al (2018) Inconel 625 lattice structures manufactured by selective laser melting (SLM): mechanical properties, deformation and failure modes. Mater Des 157:179–199. https://doi.org/10.1016/j.matdes.2018.06.010
16. Lijun X, Weidong S (2018) Additively-manufactured functionally graded Ti-6Al-4V lattice structures with high strength under static and dynamic loading: experiments. Int J Impact Eng 111:255–272. https://doi.org/10.1016/j.ijimpeng.2017.09.018
17. Tüzemen MÇ, Salamcı E, Ünal R (2022) Investigation of the relationship between flexural modulus of elasticity and functionally graded porous structures manufactured by AM. Mater Today Commun 31:103592. https://doi.org/10.1016/j.mtcomm.2022.103592
18. Kaya O, Hafizoglu H, Babacan N (2022) Effect of unit cell height on the ballistic performance of the body-centered lattice structures. Int J Innov Eng Appl 6:30–34. https://doi.org/10.46460/ijiea.1054219
19. Babacan N, Seremet H (2022) Investigation of the load-bearing capacity of Co-Cr lattice structures fabricated by selective laser melting. Int J 3D Print Tech Dig Ind 6:286–291. https://doi.org/10.46519/ij3dptdi.1139802
20. Hwang WJ, Bang GB, Choa SH (2023) Effect of a stress relief heat treatment of AlSi7Mg and AlSi10Mg alloys on mechanical and electrical properties according to silicon precipitation. Met Mater Int 29:1311–1322. https://doi.org/10.1007/s12540-022-01304-7
21. Holmen JK, Johnsen J, Jupp S et al (2013) Effects of heat treatment on the ballistic properties of AA6070 aluminium alloy. Int J Impact Eng 57:119–133. https://doi.org/10.1016/j.ijimpeng.2013.02.002
22. Hadadzadeh A, Shalchi Amirkhiz B, Odeshi A et al (2019) Role of hierarchical microstructure of additively manufactured AlSi10Mg on dynamic loading behavior. Addit Manuf 28:1–13. https://doi.org/10.1016/j.addma.2019.04.012
23. Laurençon M, de Rességuier T, Loison D et al (2019) Effects of additive manufacturing on the dynamic response of AlSi10Mg to laser shock loading. Mater Sci Eng A 748:407–417. https://doi.org/10.1016/j.msea.2019.02.001
24. Aboulkhair NT, Simonelli M, Parry L et al (2019) 3D printing of aluminium alloys: additive manufacturing of aluminium alloys using selective laser melting. Prog Mater Sci 106:100578. https://doi.org/10.1016/j.pmatsci.2019.100578
25. Kristo M, Costas M, Koenis T et al (2020) On the ballistic perforation resistance of additive manufactured AlSi10Mg aluminium plates. Int J Impact Eng 137:103476. https://doi.org/10.1016/j.ijimpeng.2019.103476
26. Nurel B, Nahmany M, Frage N et al (2018) Split Hopkinson pressure bar tests for investigating dynamic properties of additively manufactured AlSi10Mg alloy by selective laser melting. Addit Manuf 22:823–833. https://doi.org/10.1016/j.addma.2018.06.001
27. Bai L, Xu Y, Chen X et al (2021) Improved mechanical properties and energy absorption of Ti6Al4V laser powder bed fusion lattice structures using curving lattice struts. Mater Des 211:110140. https://doi.org/10.1016/j.matdes.2021.110140
28. Tancogne-Dejean T, Li X, Diamantopoulou M et al (2019) High strain rate response of additively-manufactured plate-lattices: experiments and modeling. J Dyn Behav Mater 5:361–375. https://doi.org/10.1007/s40870-019-00219-6
29. Bordin A, Imbrogno S, Rotella G et al (2015) Finite element simulation of semi-finishing turning of electron beam melted Ti6Al4V under dry and cryogenic cooling. Procedia CIRP 31:551–556. https://doi.org/10.1016/j.procir.2015.03.040
30. Ren Z, Zhang X, Wang Y et al (2021) Finite element analysis of the milling of Ti6Al4B titanium alloy laser additive manufacturing parts. Appl Sci 11:4813. https://doi.org/10.3390/app11114813
31. Uçak N, Çiçek A, Outeiro J et al (2023) Constitutive modelling of Ti6Al4V alloy fabricated by laser powder bed fusion and its application to micro cutting simulation. Mech Mater 185:104756. https://doi.org/10.1016/j.mechmat.2023.104756
32. Oymak MA, Bahçe E, Gezer İ (2024) Experimental and numerical study on micro-milling of CoCrW alloy produced by selective laser melting and casting. Proc Inst Mech Eng Part B J Eng Manuf:09544054231215107. https://doi.org/10.1177/09544054231215107
33. Scazzosi R, Giglio M, Manes A (2021) Experimental and numerical investigation on the perforation resistance of double-layered metal shield under high-velocity impact of armor-piercing projectiles. Materials 14:626. https://doi.org/10.3390/ma14030626
34. Mahbod M, Asgari M (2019) Elastic and plastic characterization of a new developed additively manufactured functionally graded porous lattice structure: analytical and numerical models. Int J Mech Sci 155:248–266. https://doi.org/10.1016/j.ijmecsci.2019.02.041
35. Gebhardt U, Gustmann T, Giebeler L et al (2022) Additively manufactured AlSi10Mg lattices – potential and limits of modelling

as-designed structures. Mater Des 220:110796. https://doi.org/10.1016/j.matdes.2022.110796
36. Radlof W, Benz C, Sander M (2021) Numerical and experimental investigations of additively manufactured lattice structures under quasi-static compression loading. Mater Des Process Commun 3:1–8. https://doi.org/10.1002/mdp2.164
37. Alomar Z, Concli F (2020) A review of the selective laser melting lattice structures and their numerical models. Adv Eng Mater 22:1–17. https://doi.org/10.1002/adem.202000611
38. Maconachie T, Leary M, Tran P et al (2022) The effect of topology on the quasi-static and dynamic behaviour of SLM AlSi10Mg lattice structures. Int J Adv Manuf Technol 118:4085–4104. https://doi.org/10.1007/s00170-021-08203-y
39. Nirmal RR, Patnaik BSV, Jayaganthan R (2021) FEM simulation of high speed impact behaviour of additively manufactured AlSi10Mg alloy. J Dyn Behav Mater 7:469–484. https://doi.org/10.1007/s40870-020-00285-1
40. Maconachie T, Leary M, Zhang J et al (2020) Effect of build orientation on the quasi-static and dynamic response of SLM AlSi10Mg. Mater Sci Eng A 788:139445. https://doi.org/10.1016/j.msea.2020.139445
41. Aktürk M, Boy M, Gupta MK et al (2021) Numerical and experimental investigations of built orientation dependent Johnson–Cook model for selective laser melting manufactured AlSi10Mg. J Mater Res Technol 15:6244–6259. https://doi.org/10.1016/j.jmrt.2021.11.062
42. Hou Y, Li Y, Cai X et al (2022) Mechanical response and response mechanism of AlSi10Mg porous structures manufactured by laser powder bed fusion: experimental, theoretical and numerical studies. Mater Sci Eng A 849:143381. https://doi.org/10.1016/j.msea.2022.143381
43. Standard test methods for tension testing of metallic materials, ASTM E8/E8M (2011). American Society for Materials and Testing, West Conshohocken.
44. Johnson GR, Cook WH (1983) A constitutive model and data for metals subjected to large strains, high strain rate, high strain rates, and high temperatures. In: Proceeding of the 7th interactional symposium on ballistics, pp 541–547
45. Murugesan M, Jung DW (2019) Johnson cook material and failure model parameters estimation of AISI-1045 medium carbon steel for metal forming applications. Materials 12:609. https://doi.org/10.3390/ma12040609
46. Cao Y, Zhen Y, Song M et al (2020) Determination of Johnson–Cook parameters and evaluation of Charpy impact test performance for X80 pipeline steel. Int J Mech Sci 179:105627. https://doi.org/10.1016/j.ijmecsci.2020.105627
47. Forni D, Mazzucato F, Valente A, Cadoni E (2021) High strain-rate behaviour of as-cast and as-build Inconel 718 alloys at elevated temperatures. Mech Mater 159:103859. https://doi.org/10.1016/j.mechmat.2021.103859
48. Johnson GR, Cook WH (1985) Fracture characteristics of three metals subjected to various strains, strain rates, temperatures and pressures. Eng Fract Mech 21:31–48. https://doi.org/10.1016/0013-7944(85)90052-9
49. Banerjee A, Dhar S, Acharyya S et al (2015) Determination of Johnson cook material and failure model constants and numerical modelling of Charpy impact test of armour steel. Mater Sci Eng A 640:200–209. https://doi.org/10.1016/j.msea.2015.05.073
50. Bridgman PW (1964) Studies in large plastic flow and fracture. Harvard University Press, Cambridge
51. Teng X, Wierzbicki T (2006) Evaluation of six fracture models in high velocity perforation. Eng Fract Mech 73:1653–1678. https://doi.org/10.1016/j.engfracmech.2006.01.009
52. Onal E, Frith JE, Jurg M et al (2018) Mechanical properties and in vitro behavior of additively manufactured and functionally graded. Metals 8:200. https://doi.org/10.3390/met8040200
53. Choy SY, Sun CN, Leong KF, Wei J (2017) Compressive properties of functionally graded lattice structures manufactured by selective laser melting. Mater Des 131:112–120. https://doi.org/10.1016/j.matdes.2017.06.006
54. Jin N, Wang F, Wang Y et al (2019) Failure and energy absorption characteristics of four lattice structures under dynamic loading. Mater Des 169:107655. https://doi.org/10.1016/j.matdes.2019.107655